Regular Article – Theoretical Physics

Prospective study on microscopic potential with Gogny interaction[⋆]

G. Blanchon[1,a], M. Dupuis[1], and H.F. Arellano[2,1]

[1] CEA, DAM, DIF F-91297 Arpajon, France
[2] Department of Physics - FCFM, University of Chile, Av. Blanco Encalada 2008, Santiago, Chile

Abstract. We present our current studies and future plans on microscopic potential based on effective nucleon-nucleon interaction and many-body theory. This framework treats in an unified way nuclear structure and reaction. It offers the opportunity to link the underlying effective interaction to nucleon scattering observables. The more consistently connected to a variety of reaction and structure experimental data the framework is, the more constrained the effective interaction will be. As a proof of concept, we present some recent results for both neutron and proton scattered from spherical target nucleus, namely ^{40}Ca, using the Gogny D1S interaction. Possible fruitful cross-talks between microscopic potential, phenomenological potential and effective interaction are exposed. We then draw some prospective plans for the forthcoming years including scattering from spherical nuclei experiencing pairing correlations, scattering from axially deformed nuclei, and new effective interaction with reaction constraints.

1 Introduction

Producing satisfactory data evaluations based solely on many-body theories and effective nucleon-nucleon (NN) interaction is a long-term project. Two keys to success are: i) robust and well-tested nuclear reaction codes, such as TALYS [1] or EMPIRE [2], flexible enough to incorporate new microscopic models and ii) microscopic inputs such as optical model potentials, nuclear level densities, γ-ray strength functions, and fission properties, all based on effective NN interaction. Advances made along this line provide more opportunities to connect the effective NN interaction to a broad body of structure and reaction data and as a matter of fact to improve its parametrization.

1.1 Nuclear energy density functional

Many-body theories based on effective NN interaction such as Hartree-Fock(-Bogolyubov) (HF(B)) for static properties and (quasiparticle-)random-phase approximation ((Q)RPA) [3] or five-dimension collective Hamiltonian (5DCH) [4] for dynamical properties have proven their ability to describe a wide range of nuclear structure observables, including binding energy, charge radius,

deformation, excitation spectrum, density and spectroscopic factors, this for nuclear masses with $A \gtrsim 5$. As an illustration of the extended reach of the method, we show in fig. 1, nuclear deformations determined within axially deformed HFB with Gogny D1S interaction all over the nuclide chart [5]. Effective theories are usually based on phenomenological parametrizations of the effective NN interaction, such as Skyrme [6,7] or Gogny forces [8–11]. In the following we mainly focus on Gogny interaction. The fit of the interaction mostly relies on connection made with structure data through the effective theory. Those constraints are then completed by physical filters coming from infinite matter calculations. Up to now, two strategies have been adopted. The first and original one uses a restricted HF model where single-particle orbitals are approximated by harmonic-oscillator wave functions for simplicity. This makes possible to determine parameter sets of the interaction from a limited number of constraints by matrix inversion and from physical filters. This strategy has been applied with success to the determination of D1 [9], D1S [10] and D1N [11] versions of Gogny interaction. Recent multiparticle-multihole configuration mixing studies [12,13] have motivated the elaboration of a generalized Gogny interaction with finite-range density, spin-orbit and tensor terms. Along that line, Gogny D2 interaction with a finite-range density term has been designed [14]. The second strategy is more based on brute force using HFB with a self-consistent account of quadrupole correlations energies within the
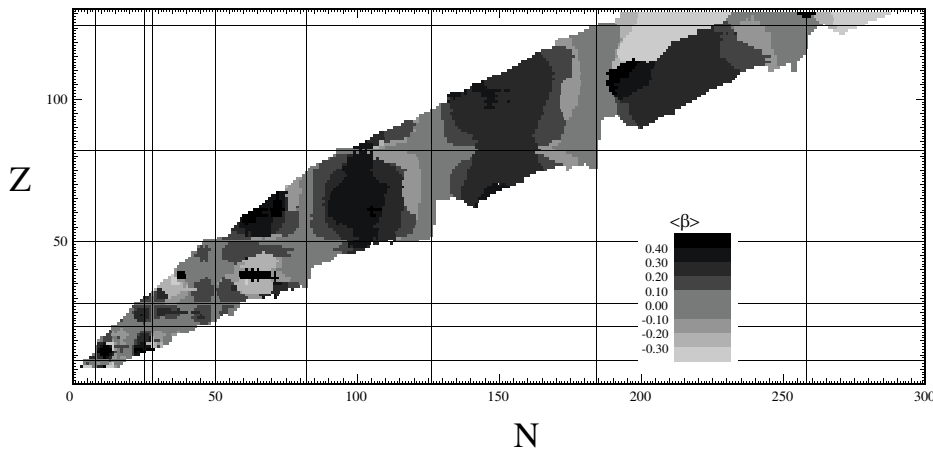
Fig. 1. Chart of the nuclides showing deformations obtained with axially deformed HFB/D1S [5].

5DCH approach. This strategy has been used to develop the D1M parametrization of Gogny interaction which reaches an rms deviation with respect to the 2149 measured masses of only 798 keV [8]. This improvement of the parametrization has been done conserving as much as possible the virtues of former Gogny interactions.

As a consequence, the global character of effective theories as well as their accuracy and their relatively low computational cost make them well suited to fulfill the needs for accurate nuclear data files in a reasonable time scale.

1.2 Nuclear codes ingredients based on effective interaction

Various phenomenological ingredients of reaction codes have been replaced by their microscopic counter parts based on effective interaction. Connecting the dots, it will be possible to obtain satisfactory evaluations on the basis of reliable and accurate microscopic inputs only [15]. A good example of this on going work is the use made of results on ^{238}U isotope described within QRPA with Gogny force [16, 17]. Those results have made possible a microscopic description of preequilibrium without *ad hoc* "pseudo-state" prescription [18]; see also Dupuis *et al.* on this issue. Along the same line, nuclear level densities have been obtained using a temperature-dependent HFB approach with Gogny interaction [19]. γ-ray strength function studies based on QRPA and Gogny interaction have also been developed [20,21]. Concerning optical potentials, TALYS uses phenomenological potentials [22,23] in the regions where data are available and a modified version of the semi-microscopic Jeukenne-Lejeune-Mahaux [24] elsewhere. Neither of those methods allows a direct connection with NN interaction. In order to fulfill this lack, we are interested in developing a microscopic potential based on the effective NN interaction.

1.3 Microscopic and ab inito potentials

Depending on the projectile energy and the target mass, various strategies have been adopted in order to deal with

elastic scattering starting from NN interaction. We now expose the pros and cons of those different methods. In the following, *ab initio* (microscopic) refers to methods based on bare (effective) NN interaction.

Nuclear matter models [25] provide reasonable descriptions of nucleon elastic scattering at incident energies above about 50 MeV [26], even up to ~ 1 GeV [27]. The method is based on the folding of a matter density and a g-matrix effective interaction built from bare NN interaction. The density is provided by an *ad hoc* prescription such as mean-field or beyond mean-field approaches. Work toward a consistent treatment of both density and g-matrix is in progress [28]. Recent *ab initio* calculations address the issue of reactions involving light nuclei and low-energy regime. The resonating group method within the no-core shell model, has successfully described nucleon scattering from light nuclei [29]. This *ab initio* model has recently been extended to include three-nucleon forces for nucleon scattering from ^{4}He [30, 31]. They deal with ^{3}He, ^{4}He and ^{10}Be targets and incident energies below 15 MeV. Another method, the Green's function Monte Carlo method has been used to describe nucleon scattering from ^{4}He in particular the phase-shift of the first partial waves below 5 MeV incident energy [32]. Other *ab initio* calculations handle magic nuclei. Among them, the self-consistent Green's function (SCGF) method has been applied to optical potential calculations for ^{40,48,60}Ca targets [33]. This method allowed to treat on the same footing particle-particle and particle-hole correlations as well as the interferences between each other [34]. The SCGF potential is compared with a phenomenological dispersive potential [35]. This model underestimates nuclear radii and, as a consequence, is not well suited for scattering calculations. Further studies including three-body forces may cure this issue. Moreover work on Gorkov-Green's function theory is in progress to extend SCGF to nuclei around closed-shell nuclei [36, 37]. Finally, the coupled-cluster theory has been applied to proton elastic scattering from ^{40}Ca [38]. Cross section at 9.6 MeV and 12.44 MeV center-of-mass energy are compared with data. They observe a lack of absorption.
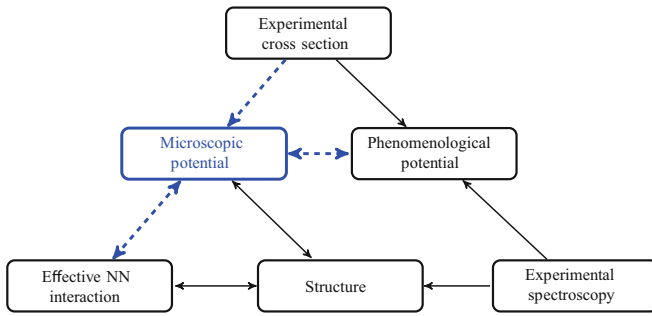
Fig. 2. Connections. Dashed arrows emphasize connections discussed in the text.

Although *ab initio* methods have made progresses in handling light and magic-nuclei, they are still not suited neither for heavy targets nor for high incident energy projectiles. Another option is to build the potential starting from an effective NN interaction. The price to pay is to break the explicit link with bare NN interaction. The advantage is once again the extended reach of effective theories and the wealth of results already available.

The so-called nuclear structure method (NSM) for scattering [39–42] relies on the self-consistent HF and RPA approximations to the microscopic optical potential [43]. The former is a mean-field potential; the latter is a polarization potential built from target nucleus excitations. This method applies to double-closed shell spherical target nuclei well described with RPA. A strictly equivalent method, the continuum particle-vibration coupling using a Skyrme interaction, has been recently applied to neutron scattering from ^{16}O [44]. They neglect part of the residual interaction in the coupling vertices. In addition, they do not address the issue of the double counting of the uncorrelated second-order diagram. Other approaches aiming at fitting a Skyrme effective interaction including reaction constraints are in progress, where optical potential is approximated as the HF term and the imaginary part of the uncorrelated particle-hole potential neglecting collectivity of target excited states [45,46]. A recent application of NSM with Gogny interaction is presented in ref. [47]. The same interaction is consistently used to generate the mean-field, the excited states and the couplings. In this study, special attention is given to the issue of the double counting of the uncorrelated second-order diagram. The subtraction of this second-order term is shown not to lead to pathological behaviors when positive incident energy is considered, contrarily to what is expected in ref. [48]. Moreover, the use of the finite-range Gogny interaction prevents from the necessity of *ad hoc* momentum cut-off when second-order effects are considered.

1.4 Project

In the continuity of work presented in ref. [47], we wish to explore the possible connections provided by a microscopic optical potential using NSM. The framework is summarized in fig. 2. In the first line of the diagram, effective interaction is used within structure models to make spec-

troscopic predictions. Feedback from experiment provides constraints on the interaction whenever a reliable structure model is used. Effective interaction and structure calculation can then be used to define the microscopic potential through NSM. Once the corresponding scattering problem is solved, feedbacks are made possible from cross section data providing reaction constraints to the fit of the interaction. Microscopic potentials are nonlocal, complex and energy dependent. They can provide prescriptions for future phenomenological potentials, in particular concerning the shape of the nonlocality and the energy dependence. One can as well investigate the origin of the volume and the surface part of the potential in terms of target excitations. Reciprocally, when data are available, phenomenological potentials can help identifying contributions missing in microscopic potentials. Moreover whenever phenomenological potentials obey dispersion relation, a connection is also made with spectroscopy. The main connections we wish to investigate in the following are highlighted in fig. 2.

The NSM formalism for spherical target nuclei and the integro-differential Schrödinger equation are briefly exposed in sect. 2.1 and sect. 2.2, respectively. In sect. 2.3, we emphasize the importance of the exact treatment of the intermediate HF propagator and more precisely the account of single-particle resonances. As a proof of concept in sect. 3, we apply NSM to nucleon elastic scattering from ^{40}Ca. Some possible cross-talks between phenomenological potentials and their microscopic counterpart are discussed in sect. 4. In sect. 5, we show how phenomenological nonlocal potential can relate to the effective NN interaction through volume integrals. Finally in sect. 6, we draw plans for the decade to come. In particular, we mention the issue of spherical target nuclei experiencing pairing correlations and the one of deformed target nuclei.

2 Method for spherical target

2.1 NSM potential

The NSM formalism is presented in detail in ref. [43]. We briefly introduce the key points of the formalism. Equations are presented omitting spin for simplicity. The NSM potential, V, consists of two components,

$$V = V^{HF} + \Delta V. \tag{1}$$

The former is a mean-field potential; the latter is a polarization potential built from target nucleus excitations. The HF potential, V^{HF}, is the major contribution to the real part of the optical potential. The polarization potential, ΔV, brings only a correction to the real part of V and entirely generates its imaginary contribution. The HF potential is obtained in the Green's function formalism neglecting two-body correlations [49]. It reads

$$V^{HF}(\mathbf{r}, \mathbf{r}') = \int d\mathbf{r}_1 v(\mathbf{r}, \mathbf{r}_1) \rho(\mathbf{r}_1) \delta(\mathbf{r} - \mathbf{r}') - v(\mathbf{r}, \mathbf{r}') \rho(\mathbf{r}, \mathbf{r}'),$$
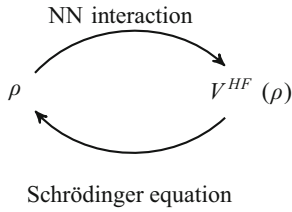
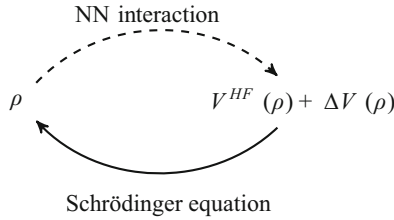$$\tag{2}$$

Fig. 3. Self-consistent Hartree-Fock.

Fig. 4. Self-consistent RPA (full-line and dashed-lined arrows). Consistent RPA on top of a self-consistent HF (full-line arrow only). The HF propagator is dressed only once.

Fig. 5. Diagrammatic contributions of V^{RPA} (a) and $V^{(2)}$ (b). Indices p, h and λ refer to particle, hole and the intermediate state in the HF field, respectively. Wavy lines stand for the effective NN interaction.

where v is the effective NN interaction and

$$\rho(\mathbf{r}) = \sum_i |\phi_i(\mathbf{r})|^2, \qquad (3)$$

$$\rho(\mathbf{r}, \mathbf{r}') = \sum_i \phi_i^*(\mathbf{r})\phi_i(\mathbf{r}'), \qquad (4)$$

are the local and nonlocal densities with i running over occupied states. V^{HF} is made of a local direct term and an exchange term which is nonlocal because of the finite range of Gogny interaction. It is energy independent and it does not bring any imaginary contribution. Rearrangement contributions stemming from the density-dependent term of the interaction are also taken into account [50]. Together with Schrödinger equation, eq. (2) defines a self-consistent scheme as shown in fig. 3.

The polarization potential, ΔV in eq. (1), is built coupling the elastic channel to the intermediate excited states of the target nucleus. Those excited states are described within the RPA formalism. Both excited states and couplings are generated using Gogny interaction. The resulting potential is nonlocal, energy dependent and complex. In NSM, the whole absorption originates from the polarization potential. Together with Schrödinger equation, eq. (1) now defines a new self-consistent scheme, illustrated in fig. 4 when considering both full-line and dashed-line arrows. In practice, as described in fig. 4, we first converge the HF scheme, as shown in fig. 3, then we dress only once the HF propagator by coupling to the excitations of the target. This makes the scheme only consistent at that stage. Going into more details, the polarization contribution to the potential reads

$$\Delta V = V^{PP} + V^{RPA} - 2V^{(2)}, \qquad (5)$$

where V^{PP} and V^{RPA} are contributions from particle-particle and particle-hole correlations, respectively. The
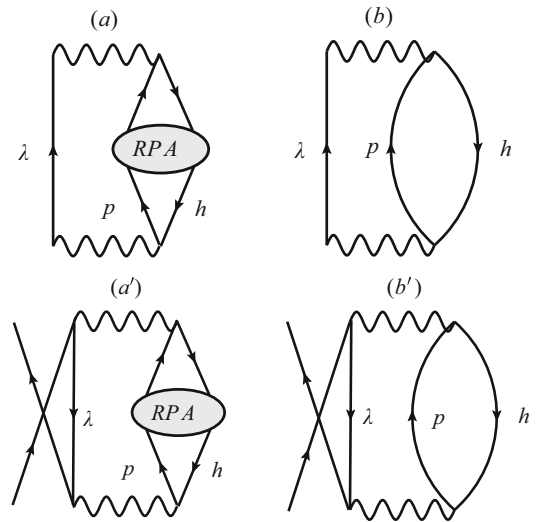
uncorrelated particle-hole contribution, $V^{(2)}$, is accounted for once in V^{PP} and twice in V^{RPA}. When two-body correlations are neglected in eq. (5), one expects ΔV to reduce to $V^{(2)}$. As a matter of fact $V^{(2)}$ shall be subtracted twice [43]. This formalism takes into account all the correlations explicitly. Although it is well suited for *ab initio* developments, we wish to make the connection with effective NN interactions. In practice, if one uses an effective interaction with a density-dependent term, such as Gogny or Skyrme forces, attention must be paid to correlations already accounted for in the interaction [41]. Indeed, in such a case, part of particle-particle correlations is already contained at the HF level. We thus use the same prescription as in ref. [40], omitting the real part of V^{PP} while approximating the imaginary part of V^{PP} by $\text{Im}[V^{(2)}]$. Then eq. (5) reduces to

$$\Delta V = \text{Im}[V^{(2)}] + V^{RPA} - 2V^{(2)}. \qquad (6)$$

Both ingredients of eq. (6), V^{RPA} and $V^{(2)}$, can be expressed in terms of diagrams. In fig. 5, wavy lines stand for the effective NN interaction and up (down) arrows stand for HF particle (hole) propagators. Subscript p (h) refers to the quantum numbers of the single-particle (hole) HF states used to build target excitations. The subscript λ refers to the quantum numbers of the intermediate single-particle state of the scattered nucleon. Both discrete and continuum spectra of the intermediate single-particle state are accounted for. Label (a) refers to V^{RPA} built with an unoccupied intermediate state. Label (a') refers to V^{RPA} built with an occupied intermediate state. Labels (b) and (b') refer to the corresponding uncorrelated particle-hole contributions. Exchange diagrams are not depicted in fig. 5 but are taken into account in the results presented in the following.

For nucleons with incident energy E, the RPA potential, corresponding to figs. 5(a) and (a′), reads

$$V^{RPA}(\mathbf{r}, \mathbf{r}', E) = \sum_{N \neq 0} \sum_{\lambda} \left[\frac{n_\lambda}{E - \varepsilon_\lambda + E_N - i\Gamma(E_N)} \right.$$
$$\left. + \frac{1 - n_\lambda}{E - \varepsilon_\lambda - E_N + i\Gamma(E_N)} \right]$$
$$\times \Omega_\lambda^N(\mathbf{r}) \Omega_\lambda^N(\mathbf{r}'), \qquad (7)$$

where n_i and ε_i are occupation number and energy of the single-particle state ϕ_i in the HF field, respectively. E_N and $\Gamma(E_N)$ represent the energy and the width of the Nth excited state of the target, respectively. Additionally,

$$\Omega_\lambda^N(\mathbf{r}) = \sum_{(p,h)} \left[X^{N,(p,h)} F_{ph\lambda}(\mathbf{r}) + Y^{N,(p,h)} F_{hp\lambda}(\mathbf{r}) \right],$$
$$(8)$$

where X and Y denote the usual RPA amplitudes and

$$F_{ij\lambda}(\mathbf{r}) = \int d^3\mathbf{r}_1 \phi_i^*(\mathbf{r}_1) v(\mathbf{r}, \mathbf{r}_1) \left[1 - \hat{P} \right] \phi_\lambda(\mathbf{r}) \phi_j(\mathbf{r}_1), \quad (9)$$

where $\hat{P}$ is a particle-exchange operator and v is the same effective NN interaction as in eq. (2). The uncorrelated particle-hole contribution, corresponding to figs. 5(b) and (b′), reads

$$V^{(2)}(\mathbf{r}, \mathbf{r}', E) = \frac{1}{2} \sum_{ij} \sum_{\lambda} \left[\frac{n_i(1 - n_j)n_\lambda}{E - \varepsilon_\lambda + E_{ij} - i\Gamma(E_{ij})} \right.$$
$$\left. + \frac{n_j(1 - n_i)(1 - n_\lambda)}{E - \varepsilon_\lambda - E_{ij} + i\Gamma(E_{ij})} \right]$$
$$\times F_{ij\lambda}(\mathbf{r}) F_{ij\lambda}^*(\mathbf{r}'), \qquad (10)$$

with $E_{ij} = \varepsilon_i - \varepsilon_j$, the uncorrelated particle-hole energy.

In practice, V^{HF} is determined in coordinate space to ensure the correct asymptotic behavior of single-particle states. This nonlocal potential is then used to build the single-particle intermediate state used to determine the polarization potential, ΔV. It is worth mentioning that the HF potential in coordinate space reproduces bound state energies obtained with the HF/D1S code on oscillator basis which makes our result reliable.

The description of target excitations is obtained solving RPA equations in a harmonic oscillator basis, including fifteen major shells [51] and using the Gogny D1S interaction [10]. We account for RPA excited states with spin up to $J = 8$, including both parities, in order to achieve the convergence of cross section calculations. The first $J^\pi = 1^-$ excited state obtained with RPA, containing the spurious translational mode, is removed from the calculation. Moreover, in order to avoid spurious modes in the uncorrelated particle-hole term, we approximate the $J^\pi = 1^-$ contribution in $V^{(2)}$ by half that of the $J^\pi = 1^-$ contribution in V^{RPA}. Indeed if one approximates $V^{(2)} \approx V^{RPA}/2$, then eq. (5) reduces to

$$\Delta V \approx \text{Im} \left[V^{RPA}/2 \right]. \qquad (11)$$

This approximation has the drawback of neglecting the real part of ΔV as well as part of the collectivity of the excited states but still yields a nice agreement with experimental cross sections. This makes this approximation well suited to bypass the issue of spurious translational modes in the $V^{(2)}$ term. An explicit removal of this spurious contribution in $V^{(2)}$ should be considered in the future following work by Mizuyama et al. [52].

Even though RPA/D1S method provides a good overall description of the spectroscopic properties of double-closed shell nuclei, still some contributions are left out. First, the projection on an oscillator basis discretizes the RPA continuum. As a consequence, the escape width, related to the correct treatment of the continuum, is missing from the structure calculation. Second, couplings to two or more particle-hole states are excluded from the model space even though they may play a significant role. The impact of these couplings is a strength redistribution through a damping width as well as a shift in energy of excited states. Third, the optical potential is, by definition, built to provide the energy-averaged S-matrix [53]. Hence, the rapid fluctuations, the potential exhibits at low energy due to compound-elastic contributions, shall be averaged before identifying the result of eq. (1) with an optical potential [54].

In the present work, we simulate those three different widths assigning a single phenomenological width, $\Gamma(E_N)$, to each RPA state. $\Gamma(E_N)$ takes the value of 2, 5, 15 and 50 MeV, for excitation energies of 20, 50, 100 and 200 MeV, respectively. Those values have not been fitted in order to better reproduce cross section data. In sect. 3, we study how cross sections are sensitive to the choice of width. Longer-term solutions are planned in order to provide more microscopic prescriptions for those widths. The escape width can be obtained using continuum RPA [44, 55]. We also plan to determine the damping width and the energy shift using the multiparticle-multihole configuration mixing method [56].

2.2 Integro-differential Schrödinger equation

The integro-differential Schrödinger equation for bound states and scattering is solved without localization procedures. The radial Schrödinger equation reads

$$-\frac{\hbar^2}{2\mu} \left[\frac{d^2}{dr^2} - \frac{l(l+1)}{r^2} \right] f_{lj}(r)$$
$$+ r \int \nu_{lj}(r, r'; E) f_{lj}(r') r' dr' = E f_{lj}(r), \qquad (12)$$

where $f_{lj}(r) = r\phi_{lj}(r)$ is the partial wave for the projectile-target relative motion, E is the incident nucleon energy and $\nu_{lj}(r, r'; E)$ is defined from the multipole expansion of the nonlocal potential

$$V(\mathbf{r}\sigma, \mathbf{r}'\sigma'; E) = \sum_{ljm} \mathcal{Y}_{ljm}(\hat{\mathbf{r}}\sigma) \nu_{lj}(r, r'; E) \mathcal{Y}_{ljm}^\dagger(\hat{\mathbf{r}}'\sigma'),$$
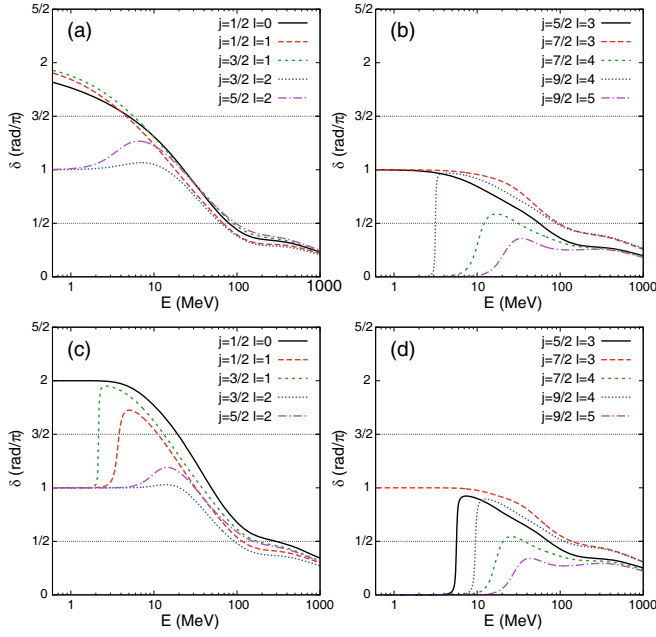$$(13)$$

Fig. 6. Phase-shift in the HF field for neutron (panels (a) and (b)) and proton (panels (c) and (d)) scattering from ^{40}Ca as a function of incident energy for the first ten partial waves.

with

$$\mathcal{Y}_{ljm}\,(\hat{\mathbf{r}}\sigma) \equiv [Y_l(\hat{\mathbf{r}}) \otimes \chi_{1/2}(\sigma)]_{jm}. \tag{14}$$

The potential, V, is complex and energy dependent for $E > 0$, and real and energy independent for $E < 0$. Discrete solutions are obtained by expressing eq. (12) on a mesh in coordinate space and performing the corresponding matrix diagonalization [57]. For positive energies, the scattering problem with the correct asymptotic conditions turns into a matrix inversion following Raynal's method for scattering exposed in the DWBA code explanatory leaflet [58].

2.3 Resonances in the intermediate wave

We now would like to emphasize the impact of an exact treatment of ϕ_λ on the second-order terms of the potential, V^{RPA} and $V^{(2)}$ (see eqs. (7) through (10)); especially, the role of single-particle resonances already discussed by Rao *et al.* [59] within a phenomenological approach. In previous works, ϕ_λ has often been approximated by a plane wave for neutron and a Coulomb wave for proton [41] or discretized [40]. In this work, we include both discrete and continuum spectra of ϕ_λ determined in the HF field with the correct asymptotic solutions. Phase-shifts for neutron and proton scattering from ^{40}Ca in the HF field are shown in fig. 6. We observe single-particle resonances for several partial waves each time phase-shift increases rapidly through an odd multiple of $\pi/2$. The corresponding resonance energies are summarized in table 1. Those resonances will result into fluctuations of the imaginary part of V^{RPA} and $V^{(2)}$ (eqs. (7) and (10)) whenever the energy $E - E_N$ matches a resonance energy ε_λ of the intermediate

Table 1. HF single-particle resonance energies (in MeV) for neutron (n) and proton (p) scattering from ^{40}Ca.

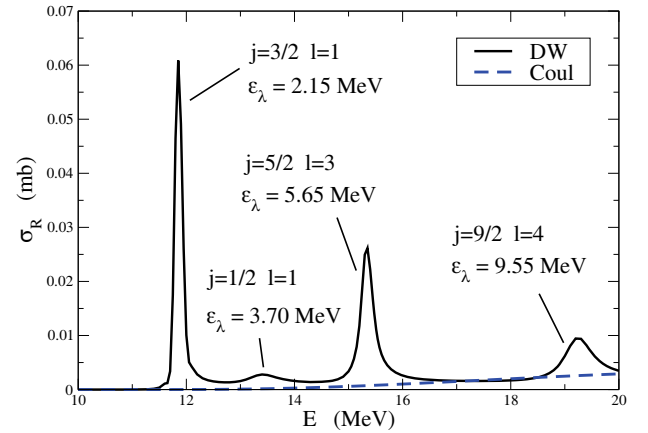| n	p
12.18 ($j = 7/2$, $l = 4$)	3.70 ($j = 1/2$, $l = 1$)
3.15 ($j = 9/2$, $l = 4$)	2.15 ($j = 3/1$, $l = 1$)
14.87 ($j = 11/2$, $l = 5$)	5.65 ($j = 5/2$, $l = 3$)
31.09 ($j = 13/2$, $l = 6$)	20.69 ($j = 7/2$, $l = 4$)
	9.55 ($j = 9/2$, $l = 4$)
	22.08 ($j = 11/2$, $l = 5$)
	39.78 ($j = 13/2$, $l = 6$)

Fig. 7. Reaction cross section *vs.* proton incident energy with $V = V^{HF} + \text{Im}[V^{RPA}/2]$ coupling only to the first 1^- excited state in ^{40}Ca ($E_x = 9.7$ MeV). Comparison between ϕ_λ treated as a Coulomb (Coul) wave (dashed line) or as a distorted wave (DW) in the HF field (solid line).

single-particle state. As a consequence, those resonances will strongly influence the corresponding cross section. As an illustration of resonance effects, in fig. 7 we show the reaction cross section for proton scattering as a function of the energy of the projectile. The potential includes the HF potential as real part and the imaginary part of the RPA potential, restricting couplings to the second $J^\pi = 1^-$ excited state of ^{40}Ca, with $E_x = 9.7$ MeV excitation energy. This is done taking $\Gamma(E_N) = 0$ MeV in eq. (7) in order to emphasize the effect of resonances. This result is compared with a calculation using a Coulomb wave as intermediate state. The exact treatment of the intermediate state leads to a global enhancement of the reaction cross section. Each bump in the reaction cross section is related to one of the intermediate single-particle resonances listed in table 1. Moreover we notice that coupling to only one excited state of the target already leads to four resonances between 10 and 20 MeV. One expects to get a large number of resonant contributions once coupling to the thousand target excited states. As an example, we show in fig. 8 the same calculation as in fig. 7 but including all the open channels for a given incident energy. Once again as discussed in sect. 2.1, one needs to average fluctuating contributions before comparing scattering observables with experiment. This shows the importance of a complete treatment of the intermediate wave.
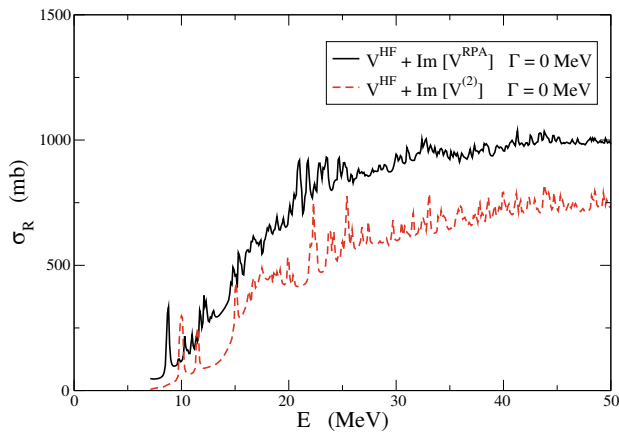
Fig. 8. Reaction cross section *vs.* neutron incident energy. Neutron scattering from ^{40}Ca with $V^{HF} + \text{Im}[V^{RPA}]$ (solid line) and $V^{HF} + \text{Im}[V^{(2)}]$ (dashed line) coupling to all available open channels and assuming zero-width RPA states.

2.4 Double counting

In this study, special attention is given to the issue of double counting of the uncorrelated second-order diagram (see eq. (5)). As discussed in terms of self-energy in ref. [48], the subtraction of the second-order term leads to unphysical results such as negative occupation numbers in the discrete part as well as negative cross sections at low incident energy caused by narrow single particle resonances in the intermediate wave. An ideal determination of the self-energy requires a consistent treatment of escape and damping widths as mentioned in sect. 2.1. Those widths result in a smoothing of integral cross sections above a given incident energy (about 10 MeV for neutron scattering off ^{40}Ca). At lower energy the cross section experiences rapid fluctuations due to the formation of compound nucleus. Once again an ideal model would describe those compound nucleus states. In the present work, we look for a potential averaged in energy sticking to the usual definition of optical potential (see for example ref. [53]). This averaged potential does not allow the resolution of low-energy compound nucleus resonances. It yields the energy-averaged S-matrix. As a result, eq. (5) now implies the subtraction of two smooth functions. The obtained averaged NSM potential does not lead to pathological behaviors when positive incident energy is considered. In fig. 9, we compare the two contributions V^{RPA} and $V^{(2)}$, from eqs. (7) and (10), respectively, for neutron scattering of ^{40}Ca at 9.91 MeV. The RPA contribution is always larger than the second-order potential so that the subtraction does not imply any unphysical change of sign. Moreover, NSM potential and the cruder approximation $\Delta V \approx \text{Im}[V^{RPA}/2]$ provide very similar contributions for the real and imaginary parts of the potential [47]. This approximation bypasses the issue of double-counting and this agreement with NSM gives a strong indication of the correct behavior of NSM potential regarding this aspect.
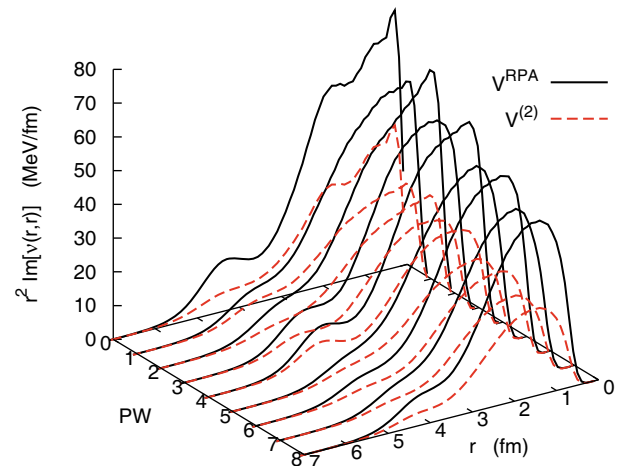

Fig. 9. Multipole expansion of the imaginary part of V^{RPA} potential (solid curve) and $V^{(2)}$ potential (dashed curve) for $r = r'$, as a function of radius r for various partial waves. $PW = 0, 1, 2, \ldots$ stand for $(l = 0, j = 1/2)$, $(l = 1, j = 1/2)$, $(l = 1, j = 3/2), \ldots$ partial waves, respectively. Neutron scattering off ^{40}Ca at 9.91 MeV is considered.

In the near future, this approximation could help in exploring compound-nucleus fluctuations within NSM.

3 Microscopic potential and cross section data

As a first application, NSM has been applied to neutron and proton scattering from ^{40}Ca using Gogny D1S interaction. The corresponding differential cross sections for incident energies below 40 MeV are presented in fig. 10. Compound-elastic corrections furnished by the Hauser-Feshbach formalism using Koning-Delaroche potential with TALYS are applied to cross sections obtained from NSM and Koning-Delaroche potential, respectively. It is mostly relevant below 10 MeV for neutron projectile while it gives a smaller contribution for proton. NSM results compare very well to experiment and those based on Koning-Delaroche potential up to about 30 MeV incident energy. References to data are given in ref. [22]. Error bars are smaller than the size symbols. Beyond 30 MeV, backward-angle cross sections are overestimated. Discrepancies at 16.9 MeV (23.5 MeV) for neutron (proton) scattering are related to resonances in the intermediate single-particle state when not completely averaged. A detailed treatment of the width might cure this issue. In fig. 11, we show calculated analyzing powers for neutron and proton scattering at several energies, in good agreement with measurements. Moreover, agreement with data is comparable to that obtained from Koning-Delaroche potential. These results suggest that NSM potential retains the correct spin-orbit behavior. In fig. 12, we show reaction cross section for proton scattering and total cross section for neutron scattering. Calculated reaction cross sections are in good agreement with experiments. For neutrons, however, we underestimate the total cross section
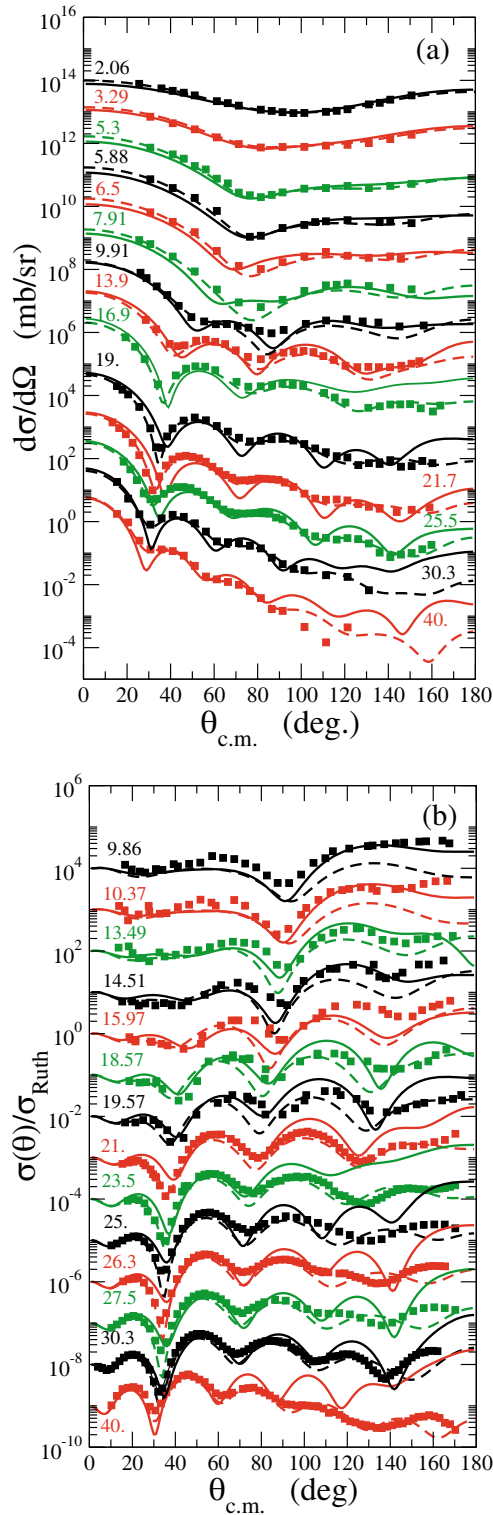
Fig. 10. Differential cross sections for neutron (a) and cross sections divided by Rutherford cross section for proton (b) scattering off ^{40}Ca. Comparison between data (symbols), NSM results (solid curves) and Koning-Delaroche potential results (dashed curves). Incident energies are indicated in MeV on the plot.
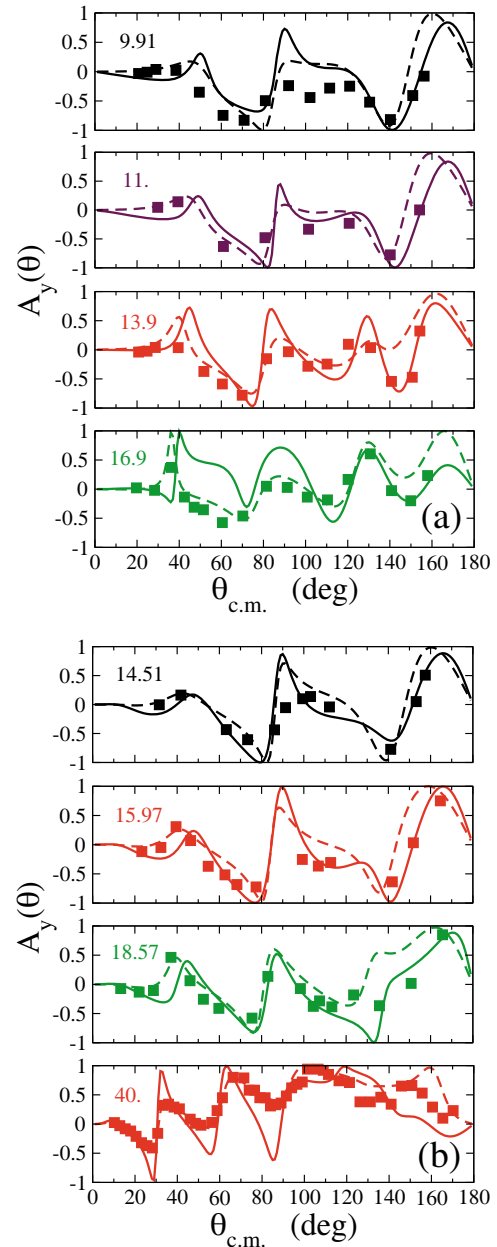

Fig. 11. Same as fig. 10 for analyzing powers.

below 10 MeV. Considering that the differential elastic cross sections are well reproduced (see fig. 10(a)), this underestimation suggests that part of absorption mechanisms is not accounted for, by target-excited states beyond RPA, double-charge exchange process or an intermediate deuteron formation.

We now study the variations of the total cross section for various prescriptions of the width $\Gamma(E)$ (see eqs. (7) and (10)) in the case of neutron scattering off ^{40}Ca. Starting from the phenomenological width described in sect. 2.1, a 20% variation of the width leads to a 3% variation of the total cross section whereas a 40% variation of the width leads to a 5% variation of the total cross section. In fig. 13, we present the effect of a variation of ±40% of the width on the differential cross section for neutron
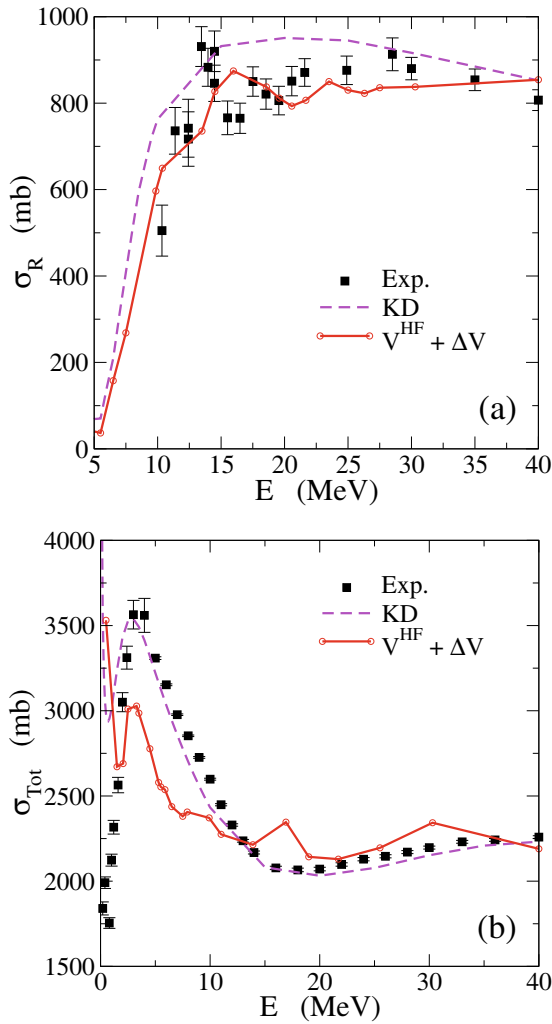
Fig. 12. Reaction cross section for proton (a) and total cross section for neutron (b) scattering from ^{40}Ca. Comparison between data (symbols), NSM results (solid curve) and Koning-Delaroche potential (dashed curve).

Fig. 13. Differential cross sections for neutron scattering off ^{40}Ca at 25.5 MeV for different values of width: $0.6 \times \Gamma$, Γ and $1.4 \times \Gamma$. Corresponding total cross sections are given.

4 Phenomenological potential and microscopic potential

We shall now highlight the possible crosstalk between microscopic and phenomenological potentials depicted in fig. 2. A large variety of local potentials have been developed in order to describe reaction data. Mahaux and Sartor have then demonstrated the need for the potential to satisfy a dispersion relation, connecting its imaginary part to its real part, which provides a link with shell model [60]. Along that line, local dispersive potentials have been developed [61,62]. One issue in those local approaches is the spurious energy dependence of the potential coming from the use of a local ansatz to represent a nonlocal object. This issue has been overcome building a dispersive potential with a nonlocal static real component [63]. A recent version of this dispersive potential is fully nonlocal both in its real and imaginary parts [64]. It is parametrized only for ^{40}Ca but using all the structure and reaction data available for this nucleus. Another nonlocal dispersive potential is currently being developed for a broader range of nuclei [65]. It is interesting to compare such phenomenological potentials with microscopic and *ab initio* ones [33,66]. This connection can help identifying missing components in microscopic potentials. Reciprocally microscopic potential can provide some guidance for next-to-come potential parametrizations regarding for example the shape and the range of the nonlocality or the incident energy dependence.

As an illustration, we now consider the case of neutron scattering from ^{40}Ca at $E = 9.91$ MeV. In fig. 14, we compare the NSM potential with the nonlocal dispersive (NLD) potential from ref. [64]. We focus on the multipole expansion (see eq. (13)) of the imaginary part of both nonlocal potentials and depict their diagonal contributions. NSM and NLD potentials compare very well around $r = 4.3$ fm at the nucleus surface. In the volume region, NSM provides a much stronger contribution to the imaginary potential than NLD potential. Nevertheless, NSM leads to a reasonable agreement with cross section data

scattering off ^{40}Ca at 25.5 MeV. Above about 10 MeV the cross section is not sensitive anymore to compound elastic processes and we can test the averaging effect of the width. As expected, a depletion (increase) of the width leads to an enhancement (reduction) of the differential cross section. Results indicate that a wide range of width is able to give a reasonable agreement with cross section data. Moreover increasing the width from Γ to $1.4 \times \Gamma$ only leads to slight changes in the differential cross section indicating that the average of single-particle resonance is accurately achieved. Further microscopic determinations of the width should provide more insight.

This microscopic potential makes the bridge between cross section data and effective interaction. It is worth mentioning that we already get nice agreement with data without any adjustable parameter and using an effective interaction, the Gogny D1S interaction, originally tailored for structure purposes. This framework opens the way for new effective interactions based both on structure and reaction constraints.
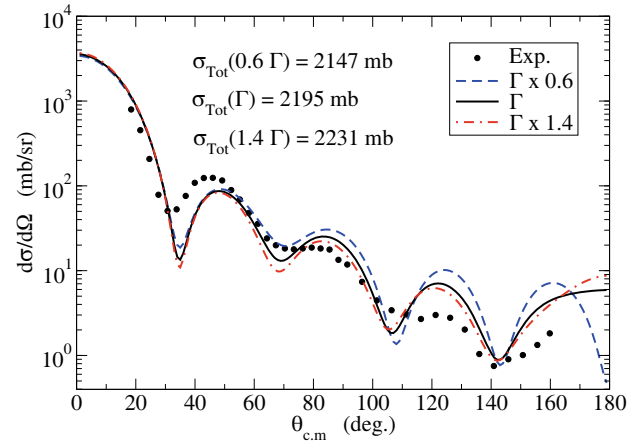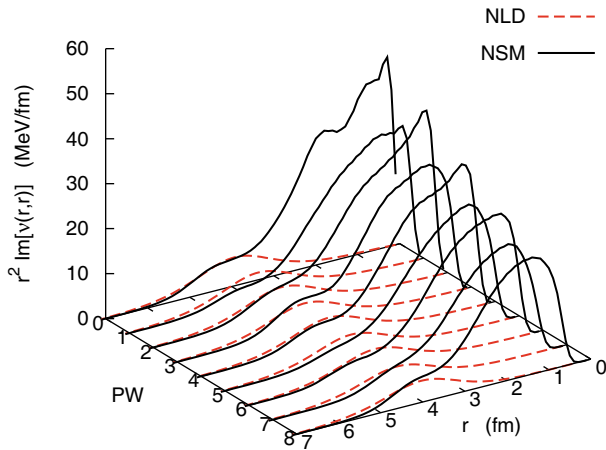
Fig. 14. Multipole expansion of the imaginary part of NSM potential (solid curve) and NLD potential (dashed curve) for $r = r'$, as a function of radius r and for various partial waves. See fig. 9 for details and notations.
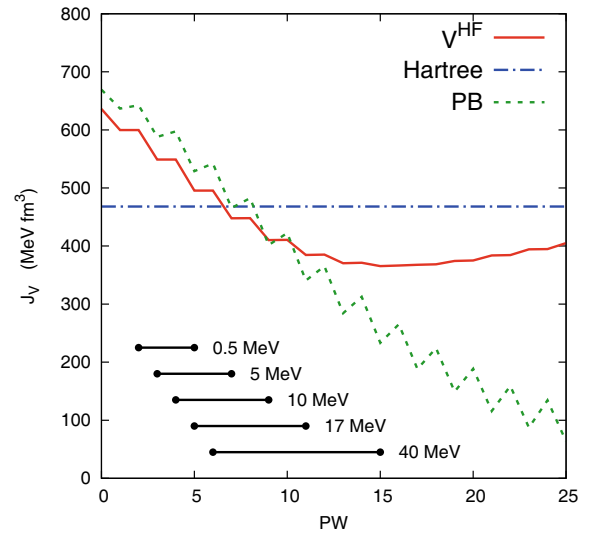

Fig. 15. Same as fig. 14 for nonlocality of the imaginary potential at $r = 4.3$ fm. $s = |\mathbf{r} - \mathbf{r}'|$ is the nonlocal parameter.

as shown in fig. 10. At relatively low incident energy the projectile nucleon is only sensitive to the surface region. In other words, low-energy elastic observables do not constrain the volume contribution of the potential. Further inelastic scattering calculations using both potentials may help disentangling this discrepancy as wave functions play a major role in such calculations. In fig. 15, we compare the nonlocality of both imaginary components at the surface of the nucleus ($r = 4.3$ fm) as a function of the nonlocal parameter $s = |\mathbf{r} - \mathbf{r}'|$. We get a good agreement between the microscopic approach and the phenomenological one. Even though small emissive contributions appear in some of the multipoles, NSM validates the choice of a Gaussian nonlocality as originally proposed by Perey and Buck [67] and used as well for NLD potential. NSM also reproduces the range of the nonlocality of the NLD potential which corresponds to a nonlocality parameter $\beta = 0.94$ fm at the surface of the nucleus.

Fig. 16. Volume integral as a function of partial waves for neutron scattering from ^{40}Ca: HF potential (solid curve), Hartree potential (dash-dotted curve) and Perey-Buck potential (dotted curve). Horizontal segments denote the partial-wave interval to sum up 80% of the reaction cross section at selected incident energies.
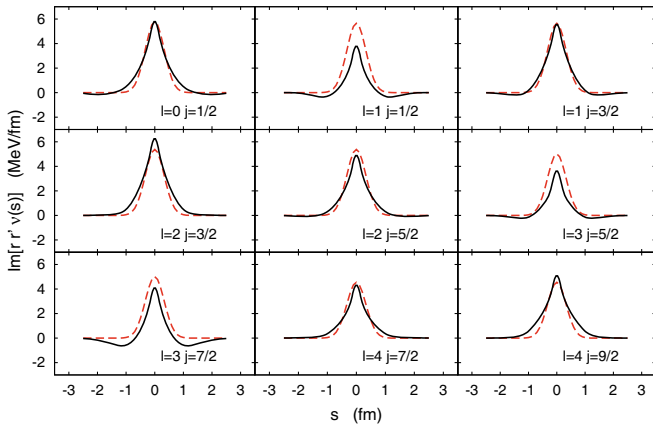
We have presented here results only for a given projectile at a given incident energy. A more exhaustive and hopefully conclusive study is in progress. Along the same line, it will be interesting to look at the nucleon asymmetry dependence of the NSM potential, for example, going toward neutron-rich Ca isotopes and comparing with the dispersive potential obtained by Charity *et al.* for ^{40,42,44,48,60,70}Ca [35].

5 Phenomenological potential and effective NN interaction

We now consider the connection between phenomenological potential and effective NN interaction through the microscopic potential and the structure calculation as shown in fig. 2. The link between microscopic potential and phenomenological one is done using volume integrals. Volume integrals are useful means of comparison between potentials as they are well constrained by scattering data. Here we focus on the real part of the potential. The volume integral for a given multipole (l, j) of the real part of the nonlocal potential is defined as,

$$J_V^{lj}(E) = \frac{-4\pi}{A} \int \mathrm{d}r \; r^2 \int \mathrm{d}r' r'^2 \, \mathrm{Re}[\nu_{lj}(r, r', E)], \quad (15)$$

where A is the nucleon number of the target. The HF potential is the leading contribution to the real part of NSM potential in eq. (1). In fig. 16, we present the volume integral of the multipole expansion of the HF potential, eq. (2), as a function of the partial wave. We compare it to the same quantity obtained from Perey-Buck (PB) non-local potential [67]. HF potential gives results similar to

PB potential up to about the twelfth partial wave. Black segments denote the strongest partial-wave contributions accounting for 80% of the reaction cross section at the selected incident energies. Hence taking the PB potential as a reference, the HF potential has a reasonable behavior up to about 17 MeV incident energy. Beyond this energy HF saturates, following the trend of the Hartree potential which is local and thus partial-wave independent. As a result increasing incident energy, HF yields a much too large volume integral reflected in an overestimate of the differential cross section at backward angles as shown in fig. 10. We present here results obtained with the D1S parametrization of the Gogny force, but we came to the same conclusions using the D1M parametrization [8]. The behavior of the volume integral as a function of the partial wave is dictated by the shape and the range of the nonlocality. PB potential is built with a Gaussian nonlocality whereas the HF potential is made of a local Hartree term and a nonlocal Fock term as shown in eq. (2). Those two contributions can be related to the different terms of the effective NN interaction, v in eq. (2). The central part of the D1S interaction contains two different finite-range components, with a Gaussian form factor, and a contact density dependent component. The contributions of those components to the Hartree potential are shown in panel (a) of fig. 17. In panel (b), we show the contributions of the two central terms with finite range to the nonlocality of the first partial wave of the Fock term. Following the shape of the finite-range components of the effective interaction, the resulting nonlocalities are Gaussian. The summation of those two nonlocalities with opposite sign yields the "W" shape of the total nonlocality. We then present in panel (c) the volume integral corresponding to the nonlocal Fock potential. The good behavior of the HF volume integral for low partial waves is related to the downward slope of the Fock volume integral and its change of sign around the seventh partial wave. Then for higher partial waves, the Fock volume integral converges to the zero limit. The corresponding behavior of the Fock term as a function of the partial wave is depicted in panel (d).

We plan to investigate to what extent the effective interaction could be improved in order to get a better behavior of the HF potential above 30 MeV. This issue emerges from the use of a local and energy-independent ersatz for the effective NN interaction instead of the actual g-matrix with its full complexity. One way to get a fully nonlocal HF potential would be to use a nonlocal effective NN interaction as proposed for example by Tabakin [68].

6 Next decade

The present work constitutes a promising step forward aimed to a model keeping at the same footing both reaction and structure aspects of the many-nucleon system. Starting from an effective NN interaction, NSM accounts reasonably well for low-energy scattering data. We use consistently the Gogny D1S interaction, although this scheme can be applied to any interaction of similar nature. An important feature of the approach is the extraction of
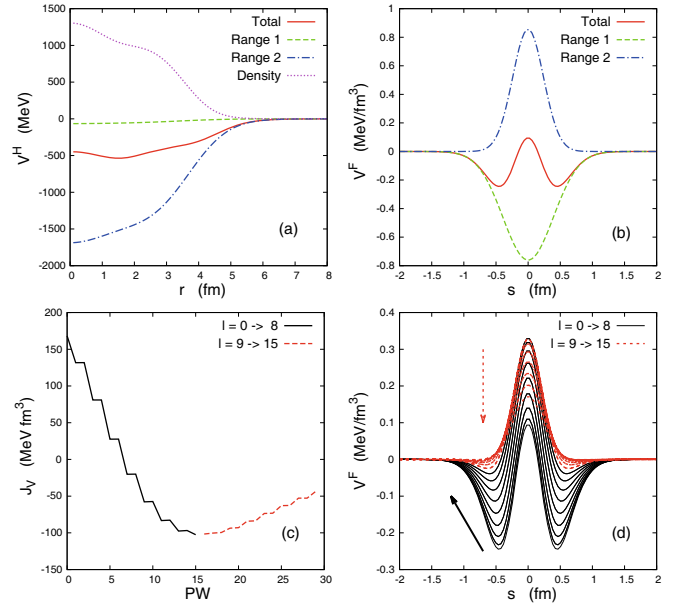

Fig. 17. Details of the V^{HF} potential for n+40Ca. (a) Decomposition of the Hartree potential with respect to the different central components of the D1S interaction: contribution of the first finite-range component, $\mu_1 = 1.2$ fm (dashed line), of the second finite-range component, $\mu_2 = 0.7$ fm (dash-dotted line), of the zero-range density-dependent term (dotted line). The sum of these three components is displayed as a solid line. (b) First partial wave of the nonlocal Fock term at $r = r' = 4.3$ fm: Total (solid line), first range of D1S (dashed line) and second range of D1S (dash-dotted line). $s = |\mathbf{r} - \mathbf{r}'|$ is the nonlocal parameter. (c) Volume integral of the Fock potential as a function of partial wave: Negative slope (solid line), positive slope (dashed line). (d) Same as (c) for the Fock components nonlocality at $r = r' = 4.3$ fm.

the imaginary part of the potential by means of intermediate excitations of the target. The study has been restricted to closed-shell target but can be extended to account for pairing correlations as well as axial deformation. We now expose in more detail our plans for the forthcoming years.

6.1 Spherical target nuclei

In the short-term future, we wish to investigate the NSM scheme for spherical targets according to the following plan:

– NSM will be applied to a broader range of target nuclei well described within RPA including ^{48}Ca, ^{90}Zr, ^{132}Sn and ^{208}Pb.

– The link between NSM potential and phenomenology can be carried on exploring energy, multipole and mass dependences of the potential. The NSM potential can also provide some trends for the shape and the range of the nonlocality. We plan to investigate the origin of surface and volume contributions as a function of target excitations.

– Above about 50 MeV incident energy, a connection can be established between the NSM potential and the folding potential relying on g-matrix and thus with the bare NN interaction. This can be a fertile ground for new effective interactions.

– At low incident energy, NSM provides a volume part of the imaginary potential larger than phenomenology. The small volume contribution in phenomenological potential is often justified by the fact that the projectile does not have sufficient energy to knock out a target nucleon. This discrepancy is possibly due to the fact that at low energy the volume part of the imaginary potential is not well constrained because the projectile does not explore the interior of the potential. We plan to use the NSM potential in inelastic scattering calculations in order to disentangle this issue.

– In its present version, NSM requires a phenomenological width. This width has several microscopic origins, as discussed in sect. 2.1. A microscopic account of those widths is planed using continuum RPA [55] and multihole-multiparticle configuration mixing [56] for the escape and the damping widths, respectively.

– The NSM potential will be used to provide transmission coefficients for compound-elastic calculations. Moreover, we plan to develop a compound-nucleus formalism based only on NSM. Indeed, NSM gives access to the fluctuating contribution of the S-matrix and as a consequence to the compound-elastic contribution.

– The study of the volume integral of the real part of the potential has exhibited the possible crosstalk between phenomenological potentials and effective NN interactions. In particular, the interaction is not well suited for the description of partial waves with more than about $\ell = 7$. Those reaction constraints will be used for new parametrizations of the interaction. Moreover, a nonlocal version of the effective NN interaction could tackle the issue of the saturation of the HF volume integral to the Hartree one.

6.2 Spherical target nuclei with pairing correlations

The main next step will be to take into account pairing correlations in spherical nuclei.

– We plan to develop a HFB potential in coordinate space. The mean-field and the pairing field have already been studied in coordinate space in a previous work on Cooper's pairs [69]. The goal is then to deal with quasiparticle scattering with a special care of resonances in both mean-field and pairing channel as shown in refs. [70,71].

– In the present approach, the intermediate particle has the same nucleonic nature than the incident and the outgoing particle. Previous studies by Osterfeld *et al.* [42] have shown the importance of double charge exchange. This process can be accounted for in a consistent way using HFB [72].

– The target excited states will then be described within QRPA [3].

6.3 Deformed target nuclei

In the midterm future, we plan to deal with axially-deformed targets according to the following plan:

– This will require the development of an axially deformed HFB potential in coordinate space. The corresponding mean field and the pairing field have already been studied in coordinate space in a previous work on Cooper's pairs [73].

– Axially deformed QRPA [3] will be used to generate excited states in the intrinsic frame of the target.

– A projection on "good" angular momentum, using the rotational approximation [74], will provide the monopole and different coupling potentials to model nucleon elastic scattering from axially deformed targets.

– The problem of solving coupled equations with nonlocal potentials will have to be addressed.

7 Conclusion

The present discussion has focused on recent advances in calculations of optical potentials from a microscopic standpoint, namely employing Gogny interaction. We have considered the example of proton and neutron scattering off ^{40}Ca as a proof-of-principle application. The results obtained through this approach compare very nicely to the existing scattering data. Comparison to more phenomenological models are also presented. We then have presented longer-term perspectives.

References

1. A.J. Koning, S. Hilaire, M. Duijvestijn, in *Proceeding of the International Conference on Nuclear Data for Science and Technology-ND2007* (EDP Sciences, Paris, 2008) pp. 211–214.
2. M. Herman, R. Capote, B. Carlson, P. Obložinský, M. Sin, A. Trkov, H. Wienke, V. Zerkin, Nucl. Data Sheets **108**, 2655 (2007) Special Issue on Evaluations of Neutron Cross Sections.
3. S. Péru, H. Goutte, Phys. Rev. C **77**, 044313 (2008).
4. J. Libert, M. Girod, J.P. Delaroche, Phys. Rev. C **60**, 054301 (1999).
5. S. Hilaire, M. Girod, Eur. Phys. J. A **33**, 237 (2007).
6. D. Vautherin, D.M. Brink, Phys. Rev. C **5**, 626 (1972).
7. M. Bender, P.H. Heenen, P.G. Reinhard, Rev. Mod. Phys. **75**, 121 (2003).
8. S. Goriely, S. Hilaire, M. Girod, S. Péru, Phys. Rev. Lett. **102**, 242501 (2009).
9. J. Dechargé, D. Gogny, Phys. Rev. C **21**, 1568 (1980).
10. J.F. Berger, M. Girod, D. Gogny, Comput. Phys. Commun. **63**, 365 (1991).
11. F. Chappert, M. Girod, S. Hilaire, Phys. Lett. B **668**, 420 (2008).

12. N. Pillet, V.G. Zelevinsky, M. Dupuis, J.F. Berger, J.M. Daugas, Phys. Rev. C **85**, 044315 (2012).
13. J. Le Bloas, N. Pillet, M. Dupuis, J.M. Daugas, L.M. Robledo, C. Robin, V.G. Zelevinsky, Phys. Rev. C **89**, 011306 (2014).
14. F. Chappert, N. Pillet, M. Girod, J.F. Berger, Phys. Rev. C **91**, 034312 (2015).
15. M. Martini, S. Hilaire, S. Goriely, A. Koning, S. Péru, Nucl. Data Sheets **118**, 273 (2014).
16. S. Péru, G. Gosselin, M. Martini, M. Dupuis, S. Hilaire, J.C. Devaux, Phys. Rev. C **83**, 014314 (2011).
17. S. Péru, M. Martini, Eur. Phys. J. A **50**, 88 (2014).
18. M. Dupuis, S. Péru, E. Bauge, T. Kawano, in *Proceeding of the 13th International Conference on Nuclear Reaction Mechanisms* (Varenna, Italy, 2012) pp. 95–100.
19. S. Hilaire, M. Girod, S. Goriely, A.J. Koning, Phys. Rev. C **86**, 064317 (2012).
20. M. Martini, S. Goriely, S. Hilaire, S. Péru, AIP Conf. Proc. **1491**, 160 (2012).
21. H.T. Nyhus, T. Renstrøm, H. Utsunomiya, S. Goriely, D.M. Filipescu, I. Gheorghe, O. Tesileanu, T. Glodariu, T. Shima, K. Takahisa *et al.*, Phys. Rev. C **91**, 015808 (2015).
22. A.J. Koning, J.P. Delaroche, Nucl. Phys. A **713**, 231 (2003).
23. E.S. Soukhovitskii, S. Chiba, J.Y. Lee, O. Iwamoto, T. Fukahori, J. Phys. G **30**, 905 (2004).
24. E. Bauge, J.P. Delaroche, M. Girod, Phys. Rev. C **63**, 024607 (2001).
25. J. Hufner, C. Mahaux, Ann. Phys. (NY) **73**, 525 (1972).
26. M. Dupuis, S. Karataglidis, E. Bauge, J.P. Delaroche, D. Gogny, Phys. Rev. C **73**, 014605 (2006).
27. H.F. Arellano, H.V. von Geramb, Phys. Rev. C **66**, 024602 (2002).
28. H.F. Arellano, private communication.
29. S. Quaglioni, P. Navrátil, Phys. Rev. Lett. **101**, 092501 (2008).
30. G. Hupin, J. Langhammer, P. Navrátil, S. Quaglioni, A. Calci, R. Roth, Phys. Rev. C **88**, 054622 (2013).
31. G. Hupin, S. Quaglioni, P. Navrátil, Phys. Rev. C **90**, 061601 (2014).
32. K.M. Nollett, S.C. Pieper, R.B. Wiringa, J. Carlson, G.M. Hale, Phys. Rev. Lett. **99**, 022502 (2007).
33. S.J. Waldecker, C. Barbieri, W.H. Dickhoff, Phys. Rev. C **84**, 034616 (2011).
34. C. Barbieri, D. Van Neck, W.H. Dickhoff, Phys. Rev. A **76**, 052503 (2007).
35. R.J. Charity, J.M. Mueller, L.G. Sobotka, W.H. Dickhoff, Phys. Rev. C **76**, 044314 (2007).
36. V. Somà, C. Barbieri, T. Duguet, Phys. Rev. C **87**, 011303 (2013).
37. V. Somà, C. Barbieri, T. Duguet, Phys. Rev. C **89**, 024323 (2014).
38. G. Hagen, N. Michel, Phys. Rev. C **86**, 021602 (2012).
39. N. Vinh Mau, A. Bouyssy, Nucl. Phys. A **257**, 189 (1976).
40. V. Bernard, N. Van Giai, Nucl. Phys. A **327**, 397 (1979).
41. A. Bouyssy, H. Ngô, N. Vinh Mau, Nucl. Phys. A **371**, 173 (1981).
42. F. Osterfeld, J. Wambach, V.A. Madsen, Phys. Rev. C **23**, 179 (1981).
43. N. Vinh Mau, *Theory of Nuclear Structure* (IAEA, Vienna, 1970) p. 931.
44. K. Mizuyama, K. Ogata, Phys. Rev. C **86**, 041603 (2012).
45. V.V. Pilipenko, V.I. Kuprikov, Phys. Rev. C **86**, 064613 (2012).
46. Y. Xu, H. Guo, Y. Han, Q. Shen, J. Phys. G: Nucl. Part. Phys. **41**, 015101 (2014).
47. G. Blanchon, M. Dupuis, H.F. Arellano, N. Vinh Mau, Phys. Rev. C **91**, 014612 (2015).
48. C. Barbieri, W.H. Dickhoff, Phys. Rev. C **63**, 034313 (2001).
49. L. Kadanoff, G. Baym, *Quantum Statistical Mechanics, Frontiers in Physics* (W.A. Benjamin, Inc., New York, 1962).
50. P. Ring, P. Schuck, *The Nuclear Many-Body Problem*, Physics and astronomy online library (Springer, 2004).
51. J. Blaizot, D. Gogny, Nucl. Phys. A **284**, 429 (1977).
52. K. Mizuyama, G. Colò, Phys. Rev. C **85**, 024307 (2012).
53. P. Hodgson, *The Nucleon Optical Potential* (Nuclear Physics Laboratory, 1983).
54. H. Feshbach, Ann. Phys. **5**, 357 (1958).
55. V. De Donno, G. Co', M. Anguiano, A.M. Lallena, Phys. Rev. C **83**, 044324 (2011).
56. N. Pillet, J.F. Berger, E. Caurier, Phys. Rev. C **78**, 024305 (2008).
57. R.H. Hooverman, Nucl. Phys. A **189**, 155 (1972).
58. J. Raynal, computer code DWBA98, 1998 (NEA 1209/05).
59. C. Rao, M. Reeves III, G. Satchler, Nucl. Phys. A **207**, 182 (1973).
60. C. Mahaux, R. Sartor, Adv. Nucl. Phys. **20**, (1991).
61. B. Morillon, P. Romain, Phys. Rev. C **70**, 014601 (2004).
62. B. Morillon, P. Romain, Phys. Rev. C **76**, 044601 (2007).
63. W.H. Dickhoff, D. Van Neck, S.J. Waldecker, R.J. Charity, L.G. Sobotka, Phys. Rev. C **82**, 054306 (2010).
64. M.H. Mahzoon, R.J. Charity, W.H. Dickhoff, H. Dussan, S.J. Waldecker, Phys. Rev. Lett. **112**, 162503 (2014).
65. B. Morillon, private communication.
66. H. Dussan, S.J. Waldecker, W.H. Dickhoff, H. Müther, A. Polls, Phys. Rev. C **84**, 044319 (2011).
67. F. Perey, B. Buck, Nucl. Phys. **32**, 353 (1962).
68. F. Tabakin, Ann. Phys. **28**, 346 (1964).
69. N. Pillet, N. Sandulescu, P. Schuck, Phys. Rev. C **76**, 024310 (2007).
70. K. Bennaceur, J. Dobaczewski, M. Płoszajczak, Phys. Rev. C **60**, 034308 (1999).
71. M. Grasso, N. Sandulescu, N. Van Giai, R.J. Liotta, Phys. Rev. C **64**, 064321 (2001).
72. M. Martini, S. Goriely, S. Péru, Nucl. Data Sheets **120**, 133 (2014).
73. N. Pillet, N. Sandulescu, P. Schuck, J.F. Berger, Phys. Rev. C **81**, 034307 (2010).
74. A. Bohr, B. Mottelson, *Nuclear Structure*, Vol. **2** (World Scientific, 1998).